A multi-technique study of “barrier layer” nano-porosity in Zr oxides during corrosion and hydrogen pickup using (S)TEM, TKD, APT and NanoSIMS

Jing Hu[1], Thomas Aarholt[1], Brian Setiadinata[1], Kexue Li[1], Alistair Garner[2], Sergio Lozano-Perez[1], Michael Moody[1], Philipp Frankel[2], Michael Preuss[2], Chris Grovenor[1]

1. Department of Materials, University of Oxford, Parks Road, Oxford, UK

2. Materials Performance Centre, School of Materials, University of Manchester, Manchester, UK

Graphic abstract:

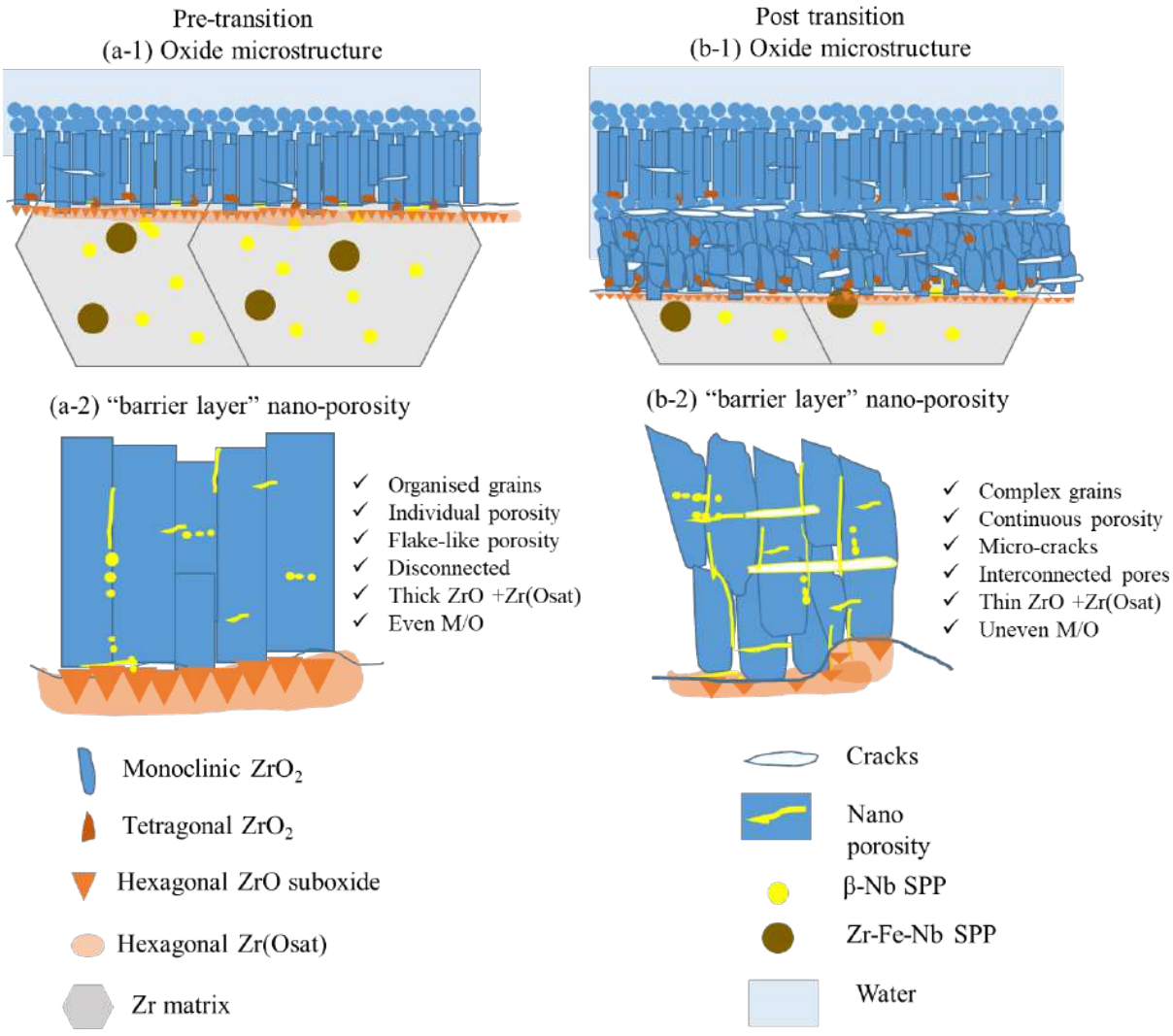

Highlights:

- Fresnel imaging in the TEM has been used to identify different types of porosity in the protective oxide near the "barrier layer", around 0~200nm from the metal-oxide interface.
- More disorganised oxide grains and nano-porosity network is found by TEM and TKD in rapidly oxidising samples.
- NanoSIMS analysis suggests that the transition event enables the propagation or trapping of deuterium while the pre-transition sample is a good barrier to deuterium penetration.
- APT data provides strong direct evidence for D segregation in the "barrier layer" at oxide grain boundaries and nano porosity.
- The nanopores, if interconnected, can be the dominant pathway for hydrogen transport to the metal matrix.

Abstract

We have used (S)TEM, TKD, NanoSIMS and APT to study nano-porosity in the oxide grown on deuterated Zr-1.0Nb and Zr-2.5Nb alloys. A detailed analysis of "barrier layer" nano-porosity by TEM and TKD has revealed that the oxide grain structure is much more disorganised and the nano-porosity network better developed in the rapidly oxidising post-transition alloy. Direct observations of the trapped deuterium (D) distributions from NanoSIMS analysis also shows much more penetration of the oxide layer post-transition. APT analysis shows that there is Fe and D segregation to some of the oxide grain boundaries with occasional evidence of porosity containing trapped D and H. We conclude that interconnected porosity would offer a dominant pathway for

the transport of hydrogenic species to the metal substrate during the aqueous corrosion of zirconium alloys in service.

Keywords:

Zr alloys, corrosion, hydrogen pickup, nano-porosity, Fresnel imaging, Transmission Kikuchi Diffraction, Atom Probe Tomography, NanoSIMS

1. Introduction

Zirconium alloy cladding isolates the nuclear fuel from water coolant in a nuclear fission reactor, but in this harsh environment experience high temperature aqueous corrosion and hydrogen pickup (HPU)[1–4]. The initial oxidation process usually shows parabolic kinetics until a critical oxide thickness (typically ~1.5-3μm) where a change of kinetics known as *transition* occurs. In the post-transition regime, the oxide no longer has a passive character and the oxidation has a characteristic cyclic, quasi-linear kinetics [5–7]. The hydrogen created by the cathodic reaction in this corrosion process is then picked up by the metal, which can deleteriously affect mechanical properties and lead to fuel failure through delayed hydride cracking (DHC) [8]. Because the formation of hydrogen is a direct consequence of the corrosion process, it is not surprising that the HPU kinetics is related to the oxidation rate, with periodic variations in instantaneous HPU rates following changes in oxidation rate [9].

Recent demands to increase the burnup of fuels and so reduce the number of fuelling cycles has led to renewed interest in developing a detailed mechanistic understanding of aqueous corrosion [9–11] and hydrogen pickup in zirconium alloys, and in the design of improved alloys. The introduction of Zr-Nb alloys has resulted in significant improvements in both the corrosion

resistance, primarily by delaying the accelerated stage of corrosion (transition), and reductions in the level of hydrogen pickup [12–17]. This improved corrosion resistance has been shown to correlate with a stronger crystallographic texture in the oxide and a more protective oxide microstructure compared to those observed in older alloys like ZIRLO® [12]. Oxidation of these different initial materials results in different oxide microstructure, oxide phases and presumably metal matrix chemistry as well [18–21]. We have explored each individual aspect of these differences in order to determine which one is the major factor to influence the rate of corrosion and HPU, with particular focus on studying the oxide microstructure and chemistry at the nanoscale.

The reason to focus on the nanoscale structure is because the key mechanisms of how O and H penetrate from the water/oxide interface through the oxide are still not well understood. Several features of the complex oxide microstructure have been suggested to offer clues to the rate-controlling mechanisms for corrosion and hydrogen pickup. Cox [22–24] tried to locate the cathodic sites in anodic oxide films of Zircaloy-2 samples by using $CuSO_4$ solutions to deposit small Cu balls. It showed most of these deposit on the sites of cracks or pores, and none on $Zr(Fe/Cr)_2$ SPPs. The authors concluded that crack and pores firstly react with steam or water, and that the oxidation reaction produces metal oxides and hydrogen. Then the accumulated hydrogen will go through an incubation period until it breaks down at the bottom of the pores and hydrogen will be absorbed by the metal. Ramasubramanian et al. suggested that H transport is via an interconnected hydroxylated pathway [25], either through interconnected porosity or oxide grain boundaries, as more recently supported by DFT calculations [26,27]. The formation of hydrogen by a cathodic reaction in the oxide requires local charge transfer and some conductivity in the oxide as emphasized by Lindgren et al[28], and also the hydrogen assisted channeling of oxygen

vacancies as part of a mechanism for the penetration of the barrier oxide by hydrogen[29]. It is possible that this same mechanism plays some role in the early stages of pore formation near the metal-oxide interface where the partial pressure of oxygen will be low. These same authors suggest that hydroxylation can also occur on pore surfaces, so that pores can trap the hydrogen gas produced by local cathodic processes. If the interconnected pores observed in the post-transition regime in our results contain hydroxyl species, especially if the pores are adjacent to grain boundaries, they might provide a dominant pathway for H transport to the metal matrix. Ni et. al [30],[31] directly observed this kind of nano-porosity in oxides on Zircaloy-4 using Fresnel contrast and found that only isolated pores were observed pre-transition at the metal-oxide interface, but later in the corrosion process that the pores became more numerous and interconnected in both lateral and vertical directions. However, there is a lack of information on the relationship between the observation of porosity and the corrosion rate in Zr-Nb alloys.

This study also attempts to define the relationship between porosity in the oxide region near the metal/oxide interface and the so-called electrochemical ‘“barrier layer”’. Previous literature refers to the concept of a “barrier layer” in two different ways. The original definition of the “barrier layer” comes from EIS experiments showing that a thin layer at the innermost part of the oxide controls the overall corrosion kinetics [32–34]. These observations were interpreted to show that the “barrier layer” is highly resistive and impervious to electrolyte, from which it must be inferred that the “barrier layer” is very dense and without porosity. While the local density is not easy to measure directly, porosity can be explored using TEM and Fresnel imaging, and together with other powerful new techniques like Transmission Kikuchi Diffraction (TKD), high resolution NanoSIMS and Atom Probe Tomography (APT) can be used to study the “barrier layer” region of oxides in unprecedented detail. In this paper we present new results obtained from these

techniques in Zr-1.0 Nb and Zr-2.5Nb alloys at different stages of corrosion (pre-transition and post-transition). We give a qualitative overview of the concentration and nature of porosity present in oxides grown on these alloys with different starting microstructures, and also link this to corrosion rate and hydrogen pick up.

2. Materials and Methods

In this study we report results on two sets of Zr-Nb alloys: Zr-1.0 Nb and Zr-2.5Nb alloys which empirically are known to reduce the hydrogen pickup fraction than other alloys such as ZIRLO®, Zircaloy-2 and Zircaloy-4. The samples are all in tube shape. The Zr-1.0Nb alloys were development materials supplied by Westinghouse in an as-recrystallised state. The composition of these alloys was measured by EDF using inductively coupled plasma atomic emission spectrometry (ICP-AES) to be Zr-0.9Nb-0.01Sn-0.08Fe (wt%). The final heat treatment for the Zr-1.0Nb alloy was carried out at 580ºC, resulting in an equiaxed grain structure and the precipitation of spherical β-Nb particles. Coupons were oxidised in an autoclave at EDF under simulated pressurised water reactor (PWR) water conditions containing lithium hydroxide and boric acid at 360°C for up to 540 days, and some samples then received an additional exposure to deuterated water for a further 45 days. The initial samples were removed after 15, 30, 45, 60, and then every 15 days to be weighed again before hydrogen content measurement using inert gas diffusion. Details of the autoclave testing, corrosion kinetics and hydrogen content measurements are reported in two recent publications from the MUZIC consortium [8,13], and summarised in Figure 1(a) and Table 1.

The Zr-1.0Nb samples selected for characterisation include 225-day (pre-transition) and 585-day (post-transition) samples. These were oxidised for 180 and 540 days in light water respectively,

before further oxidation in a heavy water autoclave for 45 days. The samples were not reweighed after the completion of the heavy water corrosion test. Although determination of transition points is not straightforward from this data, it is likely that this Zr-1.0Nb alloy is still in pre transition even at 360 days, Figure 1 (a). Judging from the weight gain of the 540-day sample, the transition should have taken place somewhere between 360-540 days.

The Zr-2.5Nb samples were pressure tube material used in Canada Deuterium Uranium (CANDU) reactors. These samples are the back of Tube F from a recent study [35]. They were processed by β-quenching followed by hot extrusion, cold working and stress relief at 400ºC for 24 hours. This heat treatment results in elongated α-Zr grains partially surrounded by a network of thin β-Zr filaments. During the stress relieving stage, β-Zr can decompose to β-Nb. This material was exposed to heavy water with the addition of lithium oxide at 335 °C [35], a slightly lower temperature than the Zr-1.0Nb samples. The samples selected for characterisation include 150 and 1040 day samples, primarily to study by NanoSIMS the distribution of deuterium in the oxide. Although the autoclave testing was carried out up to 1800 days, only 6 data points were taken in this timeframe and hence these specimens are not suitable to study the corrosion rates in any detail. Due to the lack of data points, it is also not possible to accurately determine the transition points in this material, Figure 1(b), but we suppose that transition occurs somewhere between 600-1040 days where there is a steep gradient between 600 and 1040 days, corresponding to an acceleration of oxidation rate between these two points.

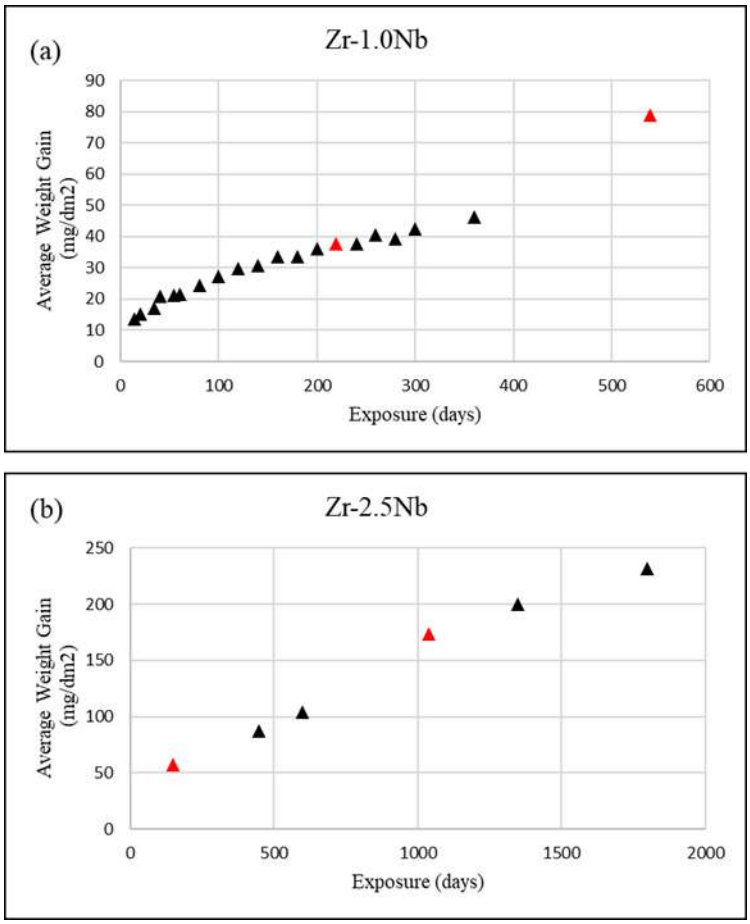

Figure 1: Weight gain data for the Zr-1.0Nb and Zr-2.5Nb samples, with samples selected for this study highlighted in red.

Table 1: Weight gain and hydrogen content data of Zr-1.0Nb and Zr-2.5Nb samples

Materials	Sample ID	Corrosion duration (days)		Corrosion Kinetics State	Corrosion weight gain (mg/dm^2)	Oxide thickness (μm)
		Light water	Heavy water			
Zr-1.0Nb (A)	A-225 (D)	180	45	Pre-transition	29.91	2.6
	A-585 (D)	540	45	Post-transition	81.34	6.1
Zr-2.5Nb (B)	B-150 (D)	0	150	Pre-transition	57.22	3.7
	B-1040 (D)	0	1040	Post-transition	173.26	8.3

TEM and APT samples were prepared using *in-situ* lift out method on a Zeiss Nvision 40 dual beam FIB with a liquid metal Ga+ ion source, with energies of 30 kV for general bulk milling, and reduced energy at 2 kV or 5 kV for removing higher-energy FIB damage from the outer edges of the sample. TEM and STEM analysis were performed on a JEOL 2100 LaB6 microscope operated at 200kV.

Transmission Kikuchi Diffraction (TKD) was performed using an FEI Magellan FEG-SEM XHR 400L operated at 30 kV with a probe current of 1.6 nA and step size of 15 nm. The transmission geometry allowed an optimal spatial resolution of ~10 nm, necessary for the study of the extremely fine oxide microstructure [36].

Atom Probe Tomography (APT) samples with tip diameter less than 100 nm were prepared for analysis near the oxide/suboxide-metal interface. All datasets in this study are obtained from laser mode atom probe analyses in a Cameca LEAP 3000X HR. Most samples were run in the

temperature range 50-55K and laser energy 0.4-0.55nJ, while the pulse frequency is maintained at 200 kHz. Data reconstruction was carried out using iVAS 3.6.6 software.

NanoSIMS analysis was carried out on a CAMECA NanoSIMS 50 with a 16 keV primary Cs+ beam. Samples cut in cross section and polished, the metal-oxide interface was imaged at a relatively low magnification to map features from the surface of the oxide and deep into the metal. As hydrogen was present in the vacuum chamber, in surface carbonacious contaminants and in the previously oxidised material, the deuterium signal can be used to show how hydrogenic species interact with the microstructure during the 45 days of heavy water oxidation in the Zr-1.0Nb samples. As deuterium is present in the environment with a natural isotopic abundance of only 0.01%, it was assumed that any significant deuterium signals detected were from the 100% heavy-water oxidation stage. We have explored the experimental conditions needed to achieve reliable analysis of deuterium in these oxidised zirconium alloy samples[37], and have used these to avoid artefacts in this work.

3. Results

3.1 TKD analysis on oxide grain structure

In order to understand the distribution of nano-porosity, it is important first to understand the grain structure of the oxide formed on these samples. Figure 2 shows a typical oxide microstructure for a series of Zr-1.0Nb alloy samples which show an even oxide thickness, rather flat metal-oxide interface, few cracks and a large spacing between layers of transition cracks (2.5~3 μm). Figure 2 (a) shows the TKD map from a 225-day pre-transition sample. The entire oxide thickness is not shown as approximately half of the oxide was lost during FIB thinning, therefore the first layer of

equiaxed grains that forms during the initial fast oxidation stage is not visible. Figure 2 (b) shows the entire oxide thickness from the 360-day sample which is believed to be near the first-transition. Figure 2 (d) shows the entire oxide thickness from the 585-day sample which has gone through two transitions since there are two layers of alternating columnar-equiaxed grains associated with two layers of the large lateral cracks, that have previously been shown to occur at transition[12].

The band contrast images from the TKD analysis shown in Figure 2 highlight the typical oxide microstructure, and agree well with the previous TEM analysis[38]. As seen in (b) and (d) which show the whole oxide thickness, the oxide starts with small equiaxed grains around 20-30 nm in diameter, and this layer is around 700 nm in thickness. Beneath the equiaxed layer, there are large, elongated columnar grains towards the metal-oxide interface, oriented parallel to the oxide growth direction. These columnar grains are around 50 nm in width and 350-450 nm in length. There are scattered parallel cracks in the pre-transition samples that break up the columnar grains. Layers of lateral cracks appear to be correlated with the transition, which is estimated to occur at about 360 days. In the 585-day post transition samples, two layers of cracks can be clearly seen, suggesting two transitions have happened. The 900 nm thick layer under the second layer of cracks contains many disorganised oxide grains that are smaller and shorter than the columnar grains formed previously around 150-200 nm in length. This may be associated with fast oxide growth after the second transition.

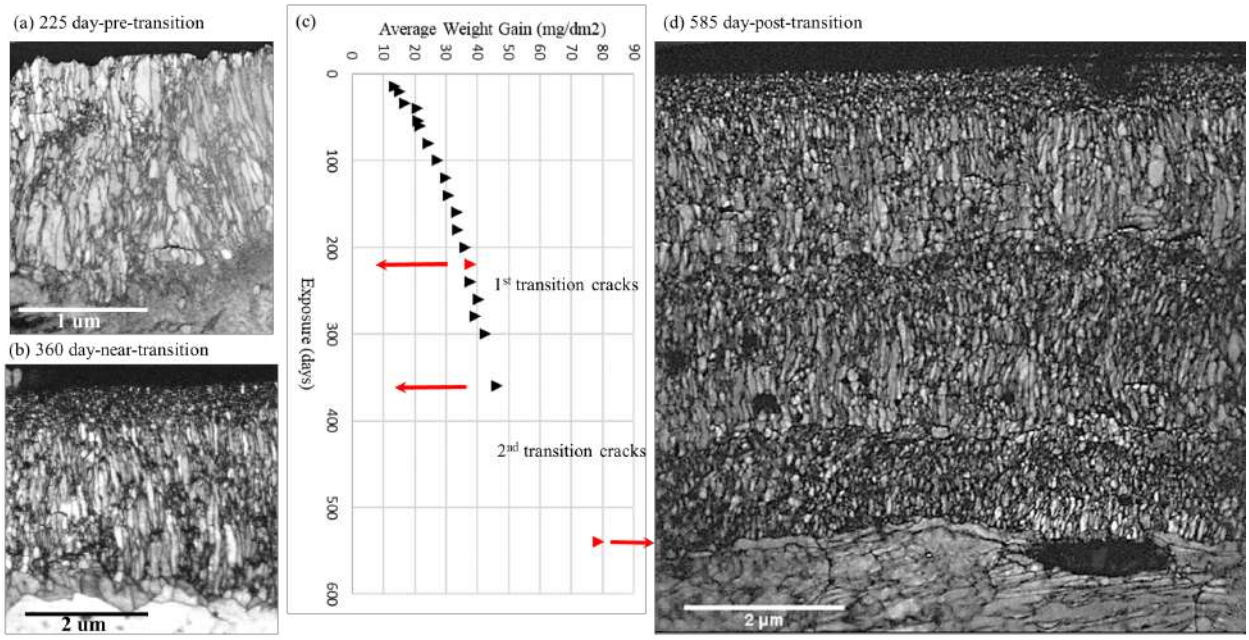

Figure 2: Oxide grain structure of typical recrystallised Zr-1.0Nb samples: TKD band contrast mapping results for (a) pre-transition 225-day sample, (b) 360-day sample, (d) post-transition 585-day sample, each sample with its weight gain is shown in (c).

3.2 NanoSIMS analysis on hydrogen distribution in oxide and metal

NanoSIMS results from the 225-day and 585-day Zr-1.0Nb show higher intensities of deuterium in the oxide than the metal as seen in Figure 3. In the 225-day sample, the strongest deuterium signals are found near the top of the oxide. These regions do not appear to coincide with cracks on this sample, in fact, no cracks were found when imaging using the NanoSIMS, although it almost certainly contains cracks that are smaller than can be resolved here. Further into the oxide the deuterium counts decrease almost to zero in the thinner regions, see the deuterium linescan in Figure 3(a) .

In the 585-day post-transition sample, the oxide thickness is very uniform. Cracks are visible in the SE images, the distribution of deuterium remains the same around the cracks as in the rest of

the oxide. Unlike the pre-transition sample, the oxide appears entirely permeated by deuterium, with the exception of a narrow band just at the metal-oxide interface which may correspond to a dense protective layer of oxide.

The metal matrix in the 225-day sample shows very low deuterium counts, whilst the 585-day sample shows regions of strong intensity which could be zirconium deuterides.

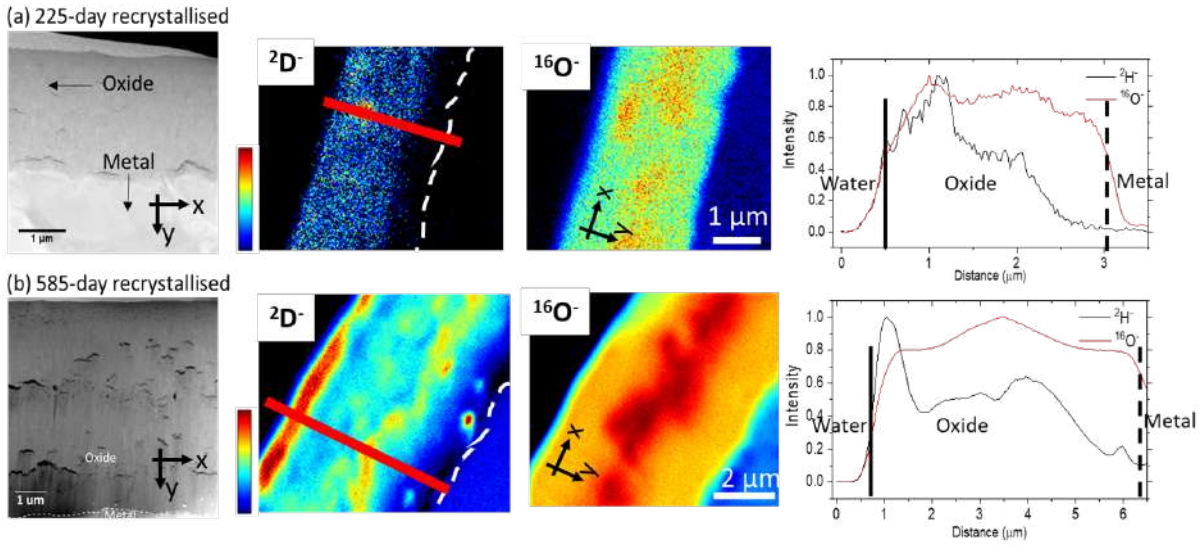

Figure 3: Typical NanoSIMS maps and line scans comparing the oxygen (Red line) and deuterium (Black line) signals from the Zr-1.0Nb (a) 225-day pre-transition and (b) 585-day post-transition. Black dashed lines show the position of the metal/oxide interface in the line profile plots. To protect the detectors, the $16O^{-}$ signal was used in the 225-day sample. The maximum value of all the line scan plots are normalized to 1.

3.3 Fresnel imaging of nano-porosity

As shown in Figure 2, different grain structures in the oxide layers can be related to the stage of the corrosion process and hence the instantaneous corrosion rate. The post-transition 585-day Zr-1.0Nb sample in Figure 2(d) has a typical oxide microstructure of equiaxed-columnar grains between the layers of transition cracks. The equiaxed grains are around 50 nm in diameter and

these regions are very porous, Figure 4 (a). These layers of equiaxed grains are frequently associated with the transient faster corrosion rate at transition and with the layers of cracks.

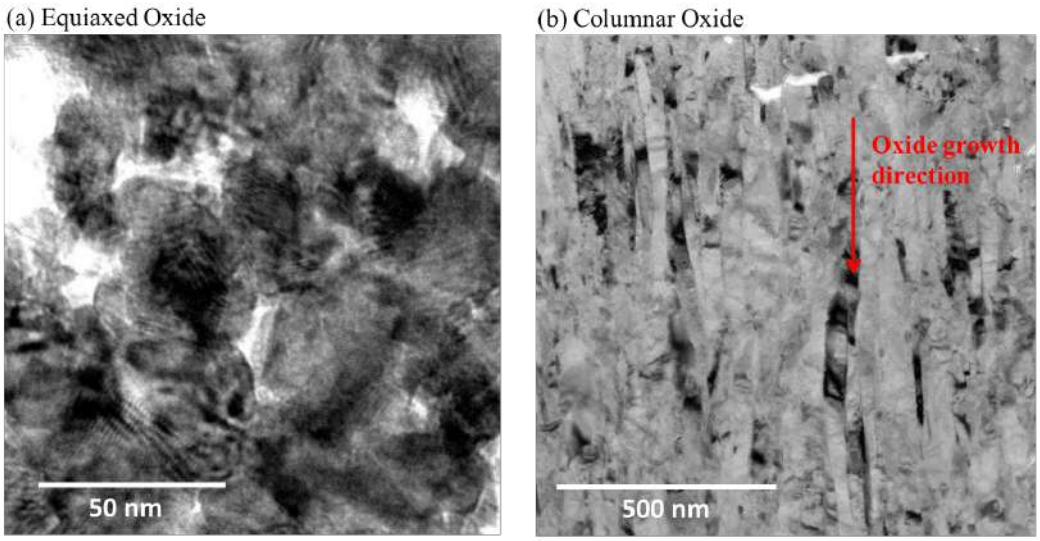

Figure 4: Oxide grain structure of a typical recrystallised Zr-1.0Nb sample: (a) TEM BF image of equiaxed grains; (b) TEM BF image of columnar grains.

The columnar grains in the oxide are very well aligned in the direction of corrosion, and the grains are around 50nm in width and 500-700 nm in length, Figure 4 (b).

Figure 5 hows that by using Fresnel contrast we are able to identify several different types of nano-porosity. In the pre-transition 225-day Zr-1.0Nb samples, nano-porosity is visible along columnar grain boundaries and we also observe small micro-cracks or flake-like porosity 20 nm in length cutting across the columnar grains. Although they are invisible in the in-focus image Figure 5(a), the nano-porosity shows bright contrast in the under focus image (b) and becomes dark in the over focus image (c). It is worth pointing out that this area is around 200 nm away from the metal-oxide interface, where the majority of the porosity is not forming an interconnected network, but is seen as individual pores.

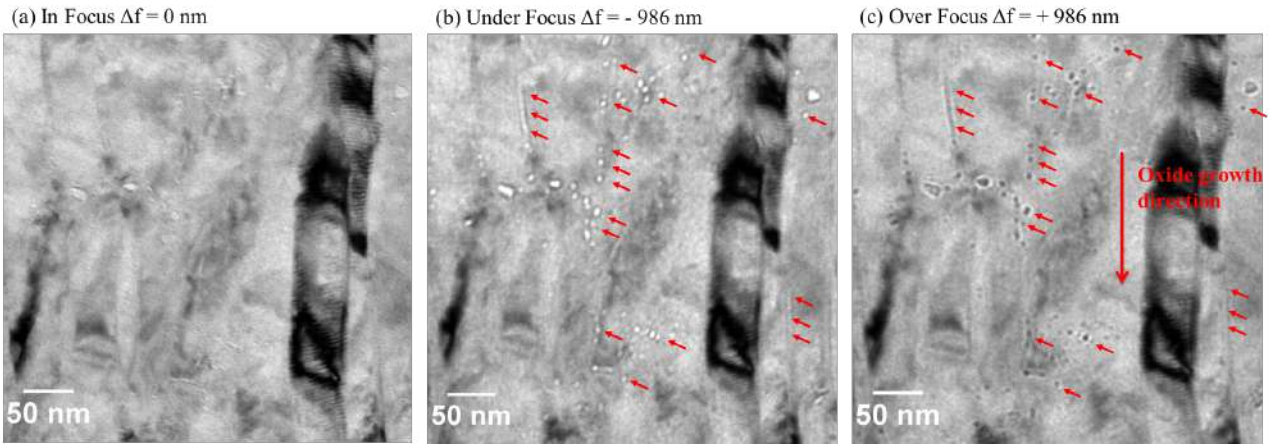

Figure 5: Fresnel image of nano-porosity in columnar oxide in 225-day pre-transition recrystallised Zr-1.0Nb around 200 nm from metal-oxide interface. (a) in focus; (b) under focus where nano-porosity is bright; (c) over focus where nano-porosity is dark.

Closer to the metal-oxide interface, where we expect to find the protective "barrier layer", there are several different types of porosity as shown in Figure 6. At ~ 100 nm from the interface, there are many individual pores, 3-5 nm in diameter, observed inside the columnar grains (Figure 6(a)), which suggests that migration through the bulk lattice is a possible path for oxygen transport in addition to the rapid transport we would expect along the porous grain boundaries. Some of the individual pores are connected in a different morphology, especially identified by circles in (a), to create an interconnected array of flake-like porosity/micro-cracking around 10-15 nm in width running parallel to the metal-oxide interface. At ~ 200 nm from the interface, some of the columnar grain boundaries are decorated with vertically interconnected porosity (b), but the pores become gradually less well connected closer the metal-oxide interface, so that individual pores are seen along the boundaries between columnar oxide grains (b). Individual pores are also observed at the metal-oxide interface (c), and particularly in the ZrO suboxide layer often observed at this interface[36], and these may act as local oxygen sinks during the

oxidation process. This is the first time that porosity in the suboxide region has been reported, and may be a result of agglomeration of the high concentration of oxygen vacancies expected near the metal-oxide interface. At the end of columnar grains in (c), there is also continuous porosity that lies immediately at the metal-oxide interface underneath the columnar grains. This type of complex interconnected porosity seems likely to play an important role in the rate determining the local oxygen diffusion processes.

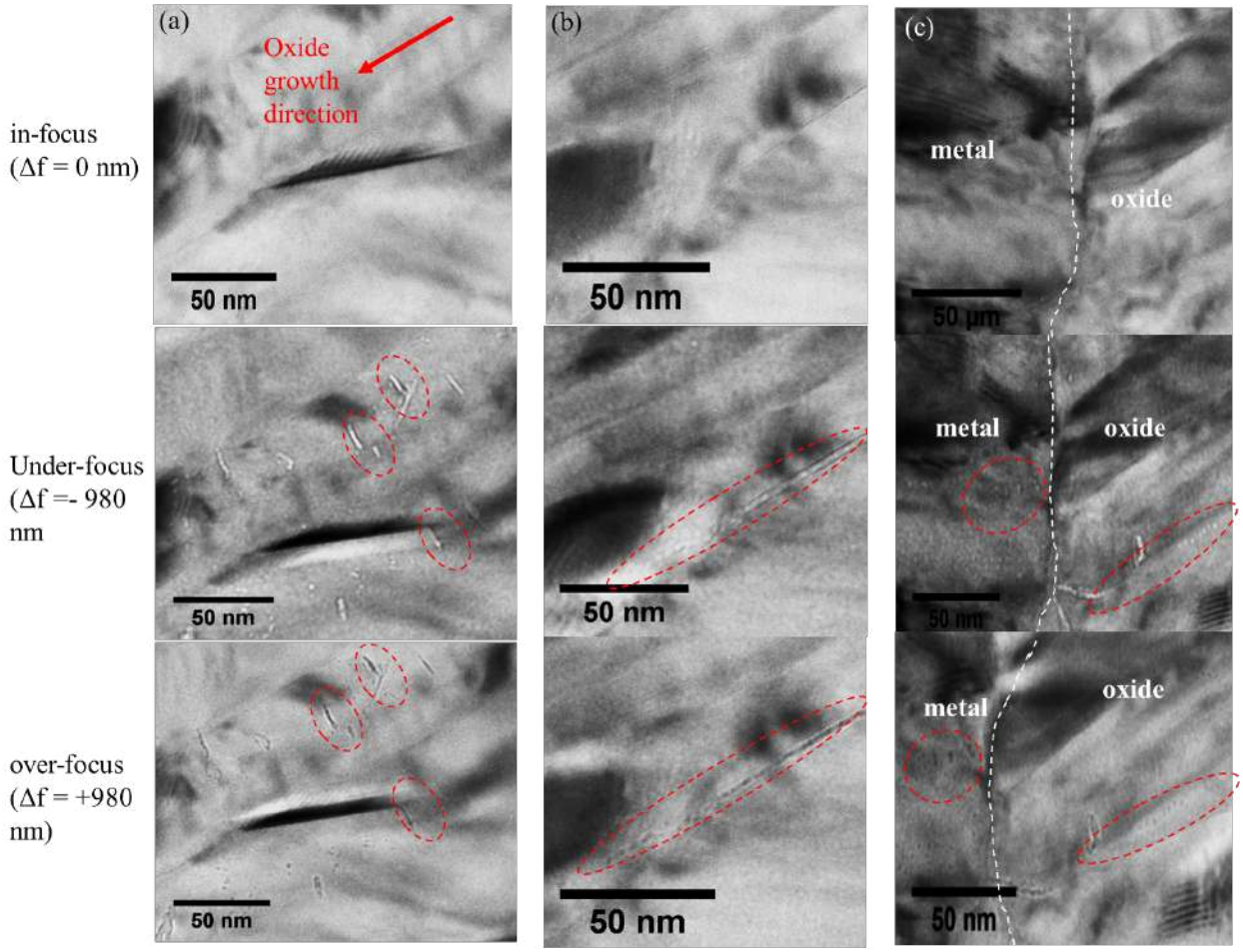

Figure 6: Through-focal imaging of fine pores (circled) close to the metal-oxide interface on the 225-day Zr-1.0Nb sample. Three different types of porosity are revealed at different locations: (a) 100 nm from the metal-oxide interface, parallel interconnected pores; (b) 100 nm from the metal-oxide interface, vertically

interconnected pores along the columnar oxide grain boundaries; (c) near the metal-oxide interface, disconnected pores and some connected porosity under the columnar grains right at the metal-oxide interface.

In order to observe the changes in the nature of the porosity as the oxide evolves, a series of Fresnel images were taken at various distances from the metal-oxide interface in the 225-day sample as shown in Figure 7. These high resolution over-focus images demonstrate the complexity of the morphology and distribution of nano-porosity in the oxide after 225 days of oxidation. Besides the individual pores and flake-like porosity in the oxide similar to those shown in Figure 6, near the water/oxide interface there is a continuous interconnected porosity along many of the columnar grain boundaries, Figure 7 (d) and near micro cracks perpendicular to the oxide growth direction, Figure 7 (h). This suggests that only the area near the metal-oxide interface is without interconnected porosity, which most likely corresponds to the previously observed ‘“barrier layer”’.

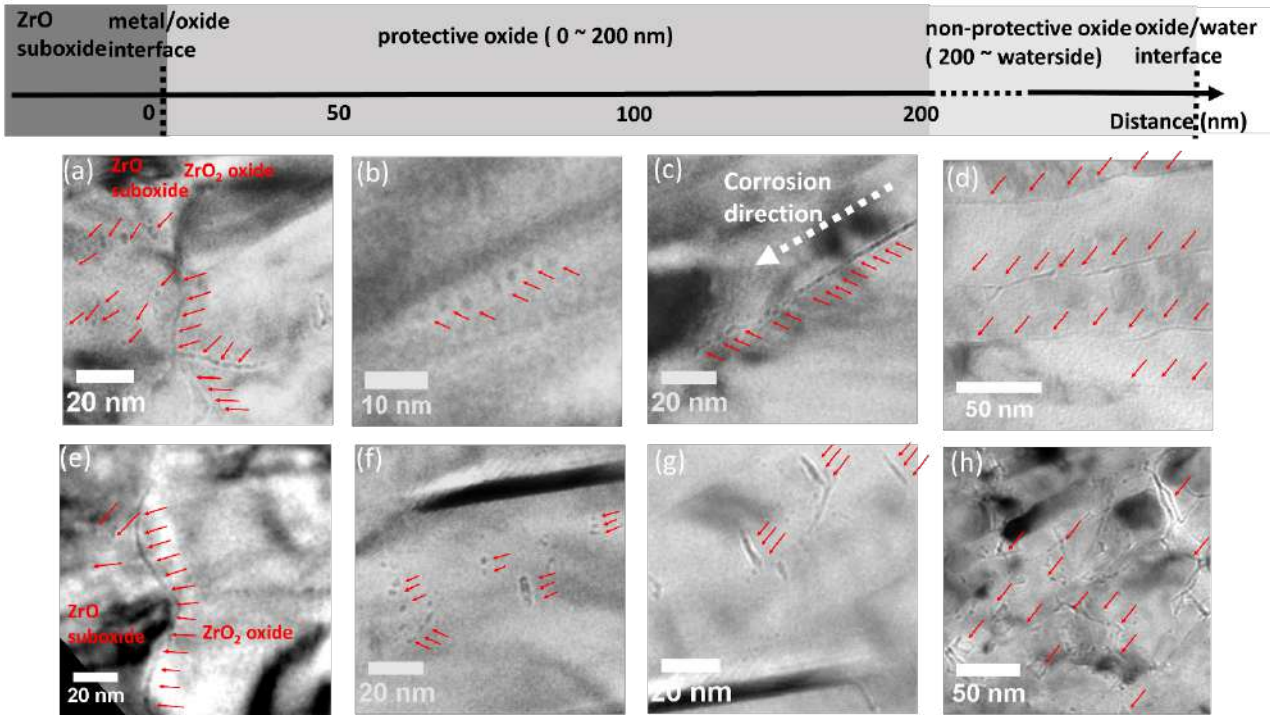

Figure 7: High resolution over-focus images of nano-porosity in the recrystallised Zr-1.0Nb sample after 225 days corrosion: (a)(e): individual pores in the suboxide, continuous pores at the oxide-suboixde interface; (b) individual pores at the columnar grain boundary; (c) vertically interconnected pores along the columnar oxide grain boundaries which gradually become disconnected to form individual pores closer to the interface; (d) continuous nano-porosity near the columnar oxide grain boundaries at the outer part of the oxide layer; (f) individual pores cutting through columnar oxide grains; (g) interconnecting flake like porosity cutting through columnar oxide grains; (h) continuous nano-porosity at the outer part of the oxide layer.

Figure 8 compares the porosity observed in oxides with different instantaneous corrosion rates, with all of the images taken less than 1 μm away from the metal-oxide interface, since this is assumed to be in or close to the electrochemical "barrier layer". In the slowing corroding 225-day pre-transition sample, Figure 8(a), the oxide microstructure is very organised with long columnar oxide grain in the TKD map (a-1) and porosity can rarely be detected at the well-aligned oxide

grain boundaries (a-2). In the faster corroding 360-day near-transition sample, Figure 8(b), the oxide structure becomes more irregular with some shorter columnar oxide grains and small equiaxed grains as indicated at the lower left side of (b-1). These grains are often decorated with a much higher density of porosity (b-2). In the fastest corroding 585-day post-transition sample (c), the oxide microstructure becomes even more disordered, with finer grains, Figure 8(c-1) and more flake-like porosity cutting through the columnar grains and forming a 3-dimensional network of porosity throughout the oxide (c-2).

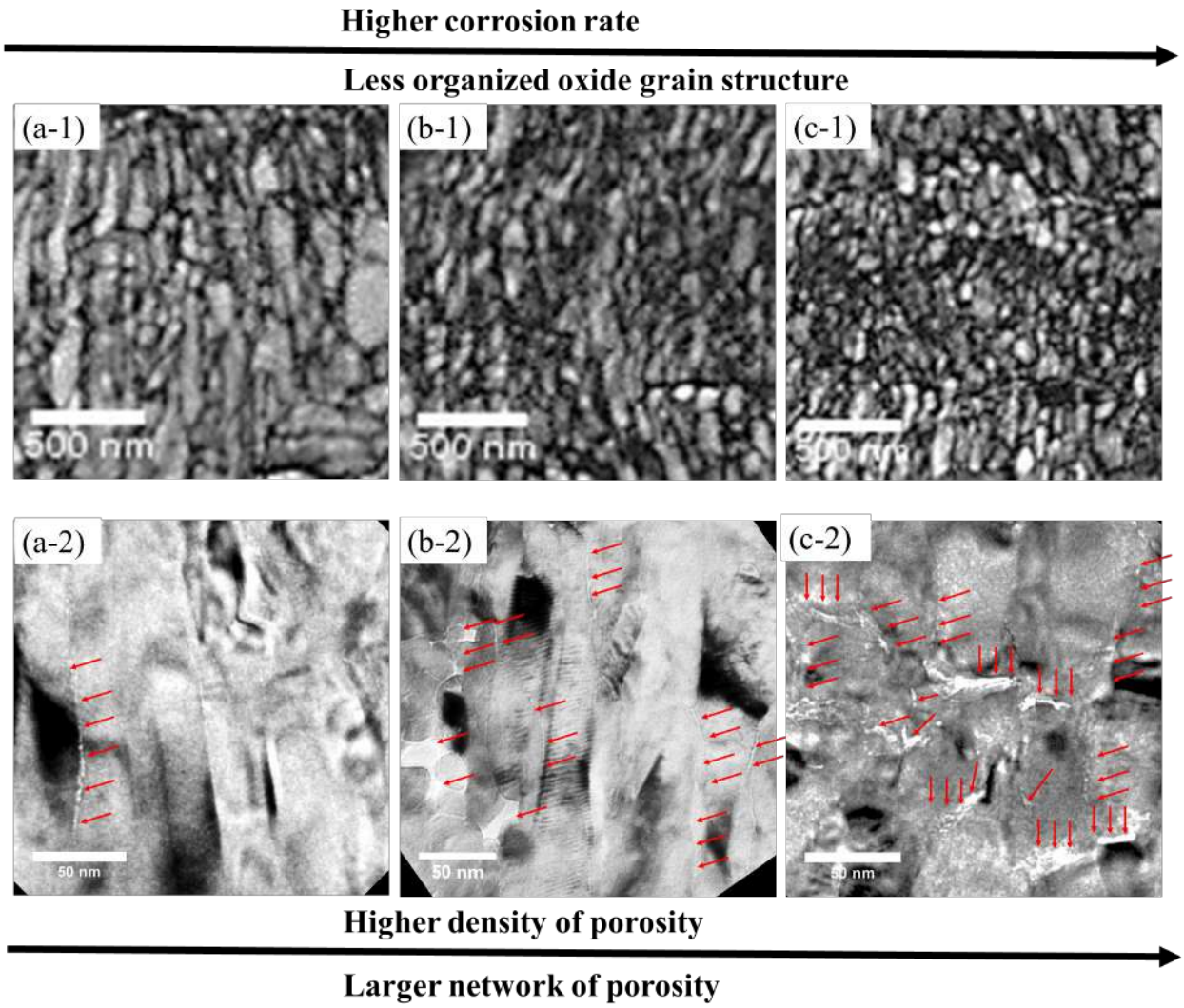

Figure 8: Comparison of porosity and grain structure as a function of corrosion rate. (a-1) (b-1) (c-1) TKD band contrast images and (a-2)(b-2)(c-2) corresponding underfocus Fresnel images (pictures all taken between 200nm and 1 um from the metal-oxide interface). (a) slowly corroding 225-day pre-transition sample; (b) faster corroding 360-day near-transition sample; (c) fastest corroding 585-day post-transition sample.

3.4 APT analysis of D/H in oxide grain boundaries

Although hydrogen detection by Atom Probe Tomography is possible, it is not straightforward. The origins of $^{1}H^{+}$ ions detected in the analysis volume is ambiguous because ambient hydrogen

cannot be excluded from the atom probe analysis chamber and during the experiment can be attracted to the surface of the cold specimen, field evaporated and ultimately detected [39,40]. Hence, it is not possible to confidently identify if the ^{1}H signal in the final reconstruction was a constituent of the original specimen or introduced from the experimental environment.

Because of these limitations with the reliable APT analysis of ^{1}H, we have used deuterium (^{2}D) as an effective surrogate to map the distribution of hydrogenic species in the microstructure. Although deuterium occurs naturally, its isotopic abundance is low (~0.015%), so if it is deliberately introduced into the treated specimen in place of hydrogen then any $^{2}D^{+}$ ions detected in the APT analysis can be interpreted with confidence as being a real signal originating from constituent atoms in the specimen, rather than being introduced from external sources [40]. The availability of samples given a second corrosion process in a heavy water autoclave provides us with material spiked with deuterium for a known time and at a defined stage of the oxidation process. The Zr-2.5Nb materials were corroded only in heavy water, and we show results below from these samples because the higher concentration of D makes segregation phenomena easier to detect. APT data sets from 2 other Zr-Nb alloy samples exposed to D-spiking for only 45 days also show very similar grain boundary and pore segregation[41].

Figure 9 shows typical APT analysis from 2 regions near the oxide/metal interface from the Zr-2.5Nb material. The existence of grain boundaries in these datasets can be inferred by the presence of planes of high atom density. This is because grain boundaries can cause trajectory aberrations that result in a focusing of the evaporated ions, leading to a region in the reconstruction with increased local atomic density compared to that of the surrounding matrix, and provides a well-established way to determine the location of grain boundaries with no elemental segregation [42]. For Analysis 1, Figure 9(a), it is clear that there are two planes with a localised, higher density of

detected atoms than the oxide matrix, and that these also correspond to the locations of high concentrations of 2Da and 18Da ions, corresponding to the detection of $^{2}D^{+}$ and $^{16}O^{2}D^{+}$ respectively. In Analysis 2, Figure 9(b), as well as similar evidence for grain boundary segregation there is a clear localised "hot spot" in the density map and an increase in the $^{2}D^{+}$ concentration at the same location.

We have carried out APT analysis on 23 datasets taken close to the metal/oxide interface, and clear evidence for deuterium segregation is observed only in 3 of these. These datasets constitute the detection of ~136 million ions that corresponds to a volume of material of ~7.10^{6} nm^{3}. Considering that the columnar oxide grain are only ~30-50 nm in width and 100-500 nm in length, and the equiaxed grains are much smaller), we can be sure that there are a significant number of grain boundaries sampled within in these datasets that show no detectable enrichment with D.

Fe atom maps are also presented because previous work on corroded Zircaloy2 samples by Sundell et al. indicated that both D and Fe can segregate to the same oxide grain boundaries [43]. However, in this study no co-segregation of D and Fe to boundary planes was observed in the data shown in Figure 9, although in Analysis 1 three small Fe clusters can be seen on the planar feature to which the D segregates.

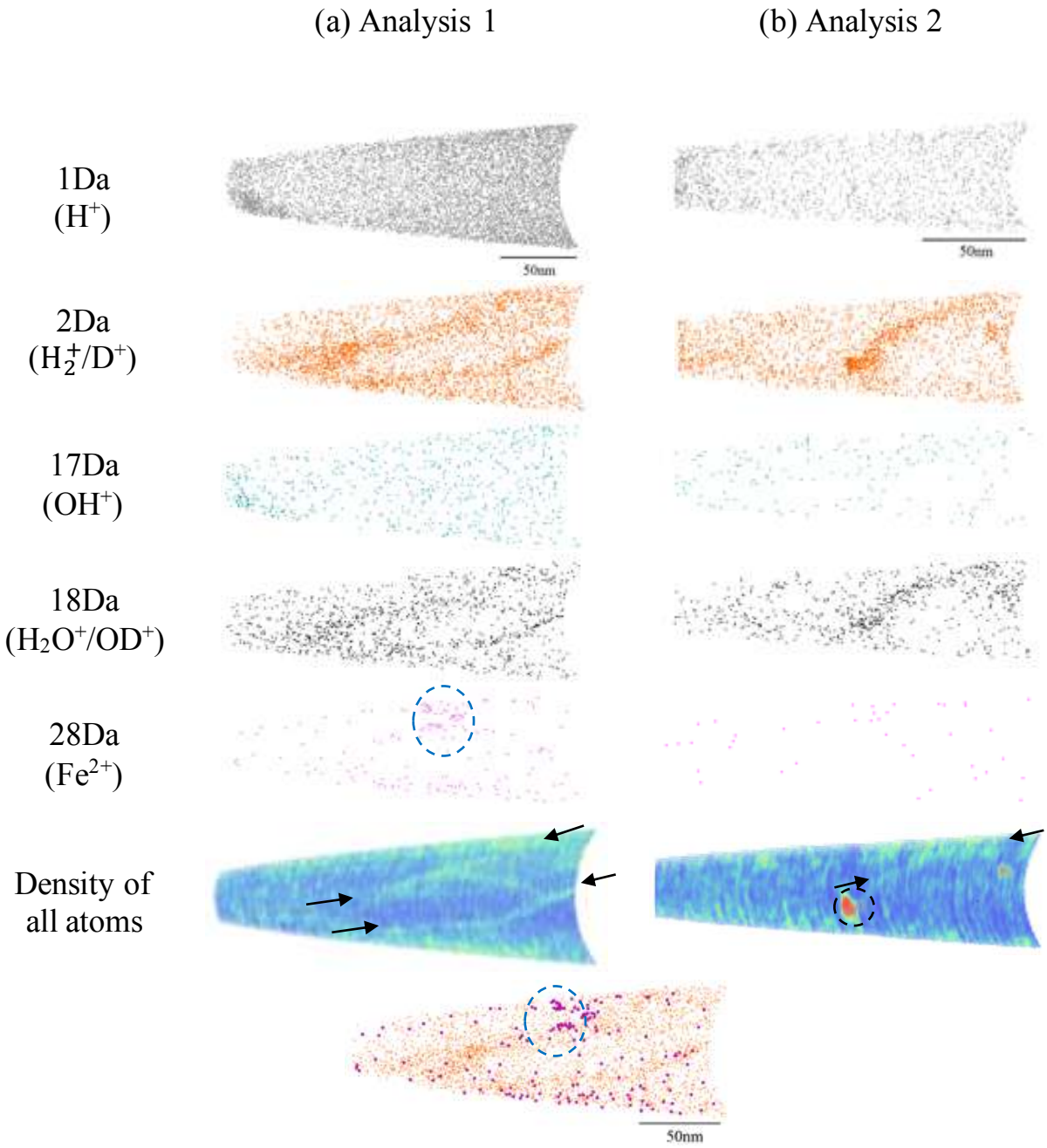

Figure 9: 10nm thick slices of APT atom reconstructions from the oxide on 2 Zr-2.5Nb samples near the M/O interface.. The atom maps show distributions of 1, 2, 17, 18, 28Da peaks and the density of all atoms. Black arrows and circles in the density maps correspond to the D-decorated oxide grain boundaries and a

possible pore. The blue circle in the Fe atom map of Analysis 1 highlights the locations of Fe clusters along a grain boundary. The location of these clusters relative to the boundary is shown in (c) where magnified Fe^{2+} ions (purple spheres) are displayed in the same atom map with 2Da ions (smaller orange dots).

Figure 10 shows another example of 3D deuterium and iron mapping in the APT, where atom map projections of planes perpendicular to the specimen axis are displayed as well as the conventional longitudinal representation at the top. It is clear from the axial projections that the 18Da (OD^+) and 28Da (Fe^{2+}) ions are strongly segregated to planar features (particularly clear in the sequence of atom maps B, C and D), but also that they do not segregate to the same locations. To confirm whether the segregation of 18Da and 28Da ions is to grain boundaries, atom density maps in the areas where these ions appear to segregate are shown in Figure 11. The planes to which 18Da and 28Da ions appear to segregate have different ion densities than the matrix, and there are atom density variations across them, suggesting that these features are indeed grain boundaries. Differential ion densities between two neighbouring grains has been observed previously in APT data [44].

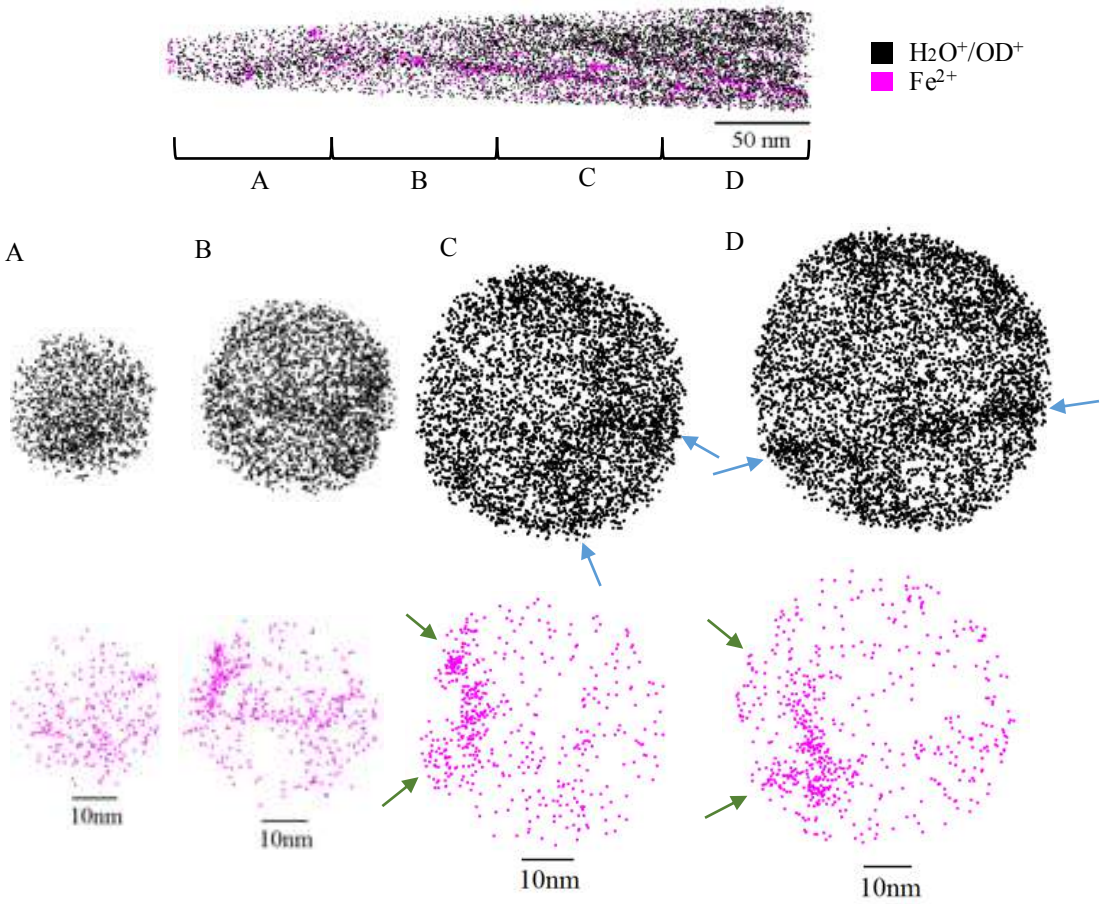

Figure 10: Slices of atom reconstructions in the plane perpendicular to the axial direction showing the distributions of 18Da (black;OD^+) and 28Da (pink;Fe^{2+}) ions. For visual clarity the ions are shown twice as large in the lower images and the blue and green arrows indicate the positions to which the 18Da and 28Da ions segregate respectively.

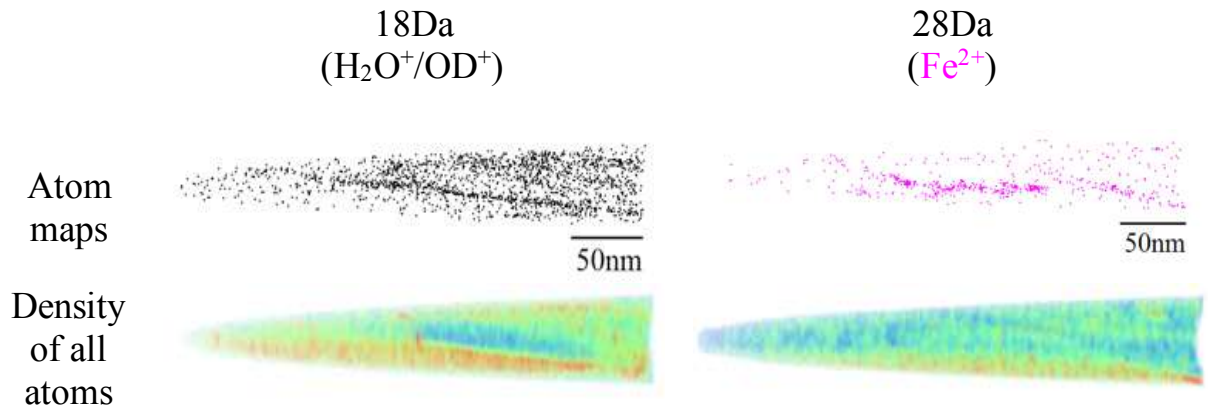

Figure 11: 10nm thick atom maps and atom density maps for the data in Figure 10 where the 18Da and 28Da peaks show segregation.

4. Discussion

4.1 Oxide growth with porosity

After examining oxides at different stages in the corrosion process using a range of complementary techniques, we can develop a better understanding of the relationship between the development of porosity and the rate of oxide growth. Based on the new experimental observations presented above, a schematic of the complex interactions occurring both pre- and post-transition is presented in Figure 12.

The TKD analysis shown in Figures 2 and 8 clearly demonstrates the different microstructure present at the different stages of oxidation. The slowly corroding pre-transition 225-day Zr-1.0Nb alloy has an extremely organised, coarse microstructure with regular equiaxed-columnar grain layers. At the metal-oxide interface, these grains are very well aligned with very few gaps/microcracks, as shown schematically in Figure 12(a-1). After transition, the fastest corroding

585-day Zr-1.0Nb has the most disorganised microstructure, with irregular, shorter columnar oxide grains as well as a higher concentration of small equiaxed grains as shown schematically in Figure 12(b-1).

The existence of nanoporosity in the oxide is well-known, especially in the outer part of the oxide layer [30,32,45,46]. In our samples, the outer oxide also has a very porous equiaxed grain structure of thickness from 150 nm towards 650 nm before the columnar oxide grains start to grow, but pores have been observed to form even in pre transition regime when the majority of the oxide is relatively dense (Figure 5, Figure 6, Figure 7). The pores are isolated in pre transition but become interconnected after transition, and many of them were also found along grain boundaries (Figure 8). These pores are thought to originate from the coalescence of vacancies in the oxide due to the Kirkendall effect and are considered to be the cause of cracks associated with transition [32,46]. This model of gradually increasing porosity as the oxide thickness increases supports the observations Ni et al [31].

This is the first time that porosity in the suboxide region has been reported, and we have seen this type of individual pores in several samples (Figure 7 (a) and (e)), but it is not surprising that it has not been reported often before because although Fresnel imaging is exactly the right technique for looking at buried nano porosity it has not been applied very often to study the metal-oxide interface. The low oxygen activity near the metal-oxide interface might be expected to lead to a high concentration of oxygen vacancies which could easily cluster or agglomerate together to form pores.

Ramasubramanian et al. suggested that H transport is via an interconnected hydroxylated pathway [25], either through interconnected porosity or oxide grain boundaries, as more recently supported

by DFT calculations [26,27]. The formation of hydrogen by a cathodic reaction in the oxide requires local charge transfer and some conductivity in the oxide as emphasized by Lindgren et al[28], and also the hydrogen assisted channeling of oxygen vacancies as part of a mechanism for the penetration of the barrier oxide by hydrogen[29]. It is possible that this same mechanism plays some role in the early stages of pore formation near the metal-oxide interface where the partial pressure of oxygen will be low. These same authors suggest that hydroxylation can also occur on pore surfaces, so that pores can trap the hydrogen gas produced by local cathodic processes. If the interconnected pores observed in the post-transition regime in our results contain hydroxyl species, especially if the pores are adjacent to grain boundaries, they might provide a dominant pathway for H transport to the metal matrix.

In this work, nano-porosity in the "barrier layer" near the metal-oxide interface has been studied in detail for the first time (Figures 6 and 7). In the pre-transition samples, some of the columnar grain boundaries near the interface are decorated with vertically connected porosity which becomes discontinuous closer to the metal-oxide interface, and become individual pores either inside the oxide grains or underneath them. Some of these individual pores seem to connect together to become micro cracks around 50-100 nm in length (Figure 7 (f) (g)), and some of these also lie directly at the metal-oxide interface (Figure 8 (c)). At transition, the individual pores become more connected, the columnar grain boundaries have more vertically connected porosity (some of which is connected with SPPs), and an interconnected network of macro-cracks form before the much longer transition cracks develop. After transition, the cycle begins again by forming isolated porosity in the new columnar oxide grains. In the second-transition samples, there is also more flake-like porosity that cuts through the columnar grains and can form a 3-dimensional network of porosity throughout the oxide with the vertical porosity along the columnar grain

boundaries. This suggests that there are more pathways for water to penetrate to the metal-oxide interface after transition. To summarise, we believe we have shown evidence that in the pre-transition stage when oxidation is slow the porosity is not interconnected. After transition when oxidation is faster, the porosity becomes interconnected.

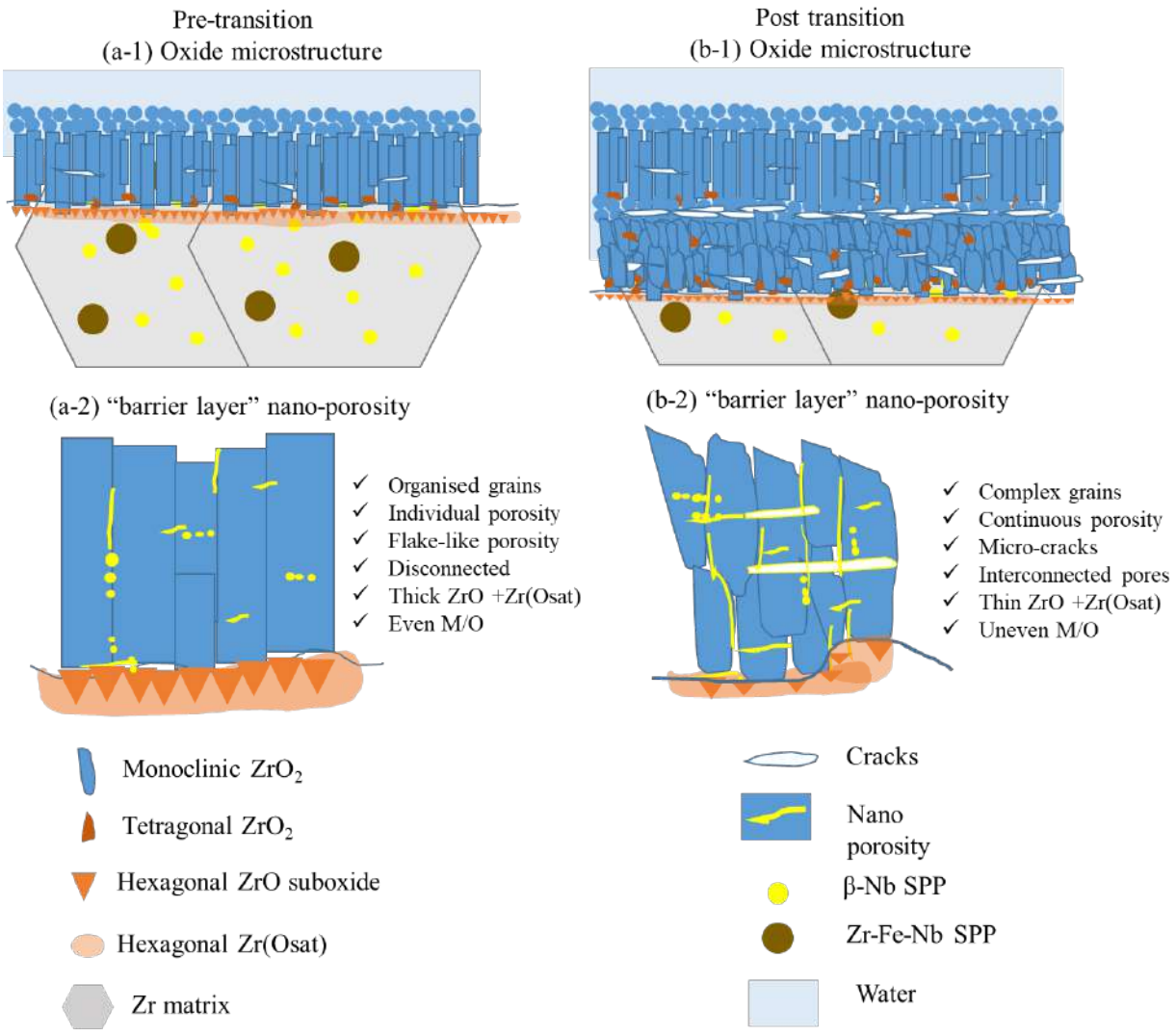

Figure 12: Schematic of the oxide structure during corrosion of Zr-1.0Nb alloys: (a-1), (b-1) oxide microstructure, (a-2) (b-2) "barrier layer" nano-porosity, (a) pre-transition, an organised equiaxed-columnar-equiaxed grain structure with little nano-porosity, (b) post-transition, more disorganised oxide grains, micro cracks and extensive nano-porosity in the oxide film.

4.2 H/D distribution with porosity

The HPU mechanism is not well understood, especially how hydrogen can migrate through the oxide layer or the locations of the cathodic reactions within the oxide. Although several hypotheses have been proposed, as discussed above, there is a lack of direct experimental data that can support them. In this study, we used deuterated samples to study the question of where the D is located within the oxide film to attempt to shed some light on the possible mechanisms for H migration.

The NanoSIMS data in Figure 3 gives an overview of D distribution in the oxide film, and shows there is a difference between pre and post transition sample in deuterium distribution. The outer region of the oxide on the deuterated alloys has been shown to have a higher deuterium concentration on both pre- and post-transition samples. In the pre-transition sample, the averaged line profile emphasises the drop in deuterium signal as it approaches the metal-oxide interface, Figure 3(a), but for the post-transition sample the outer oxide has a roughly constant intensity of deuterium signal Figure 3(b). For both samples, the oxide closest to the metal-oxide interface seems to act as a protective barrier to fast transport of deuterium during the 45 days that the samples were exposed to heavy water.

The idea that the pores in the innermost oxide function as pathways to hydrogen ingress is not new. Elmoselhi et al. [45] showed depth profiling SIMS results for deuterium concentration similar to ours, containing two regimes - a flat region in the outer oxide followed by a diffusion profile towards the metal-oxide interface. The high concentration of deuterium in the outer oxide was attributed to cracks and pores. In the APT results reported above, we have added direct evidence for D segregation at grain boundaries 500-600nm from the O/M interface which could be evidence for trapping at hydroxylated grain boundaries in this region of the oxide. In the innermost part of

the oxide, hydrogenic species may enter the metal by the rapid electrochemically-assisted process rather than directly via grain boundaries.

Hydroxylation can also occur on pores. Pores can also trap the hydrogen gas produced by the evolution process. If the interconnected pores observed in the post-transition regime contain hydroxyls, especially if the pores are adjacent to grain boundaries, they might also be a pathway for H transport. This is probably the case in Analysis 2 where a D-rich pore is observed adjacent to a grain boundary.

Although very limited experimental data has been published about the observation of pores via APT, the feature in Figure 9(b) is likely to be a pore contains significant amount of D that is probably in gaseous form or D-containing species chemisorbed on the surfaces of the pore, consistent with other reports[47,48]. In Analysis 2, next to the high density line that has been interpreted as a grain boundary, there is a highly localised region with very high atomic density (Figure 9 (b)), corresponding to the concentration of D-containing ions at 2Da and 18Da. Although, intuitively, one would expect the observation of a pore to correspond to a very low atomic density region in the APT analysis, in fact, when small pores are revealed at the surface of specimen, the opposite, as observed in this case, is more likely to be true. Upon field evaporation, the atoms surrounding the pore will most likely be subject to a trajectory aberration, focussing them inwards and creating a high density region in the APT reconstruction. This phenomenon occurs only in 2 datasets out of 23 datasets and hence is very rare. Because this spot gives such a distinct contrast in the density map, it is probably a physical feature, combined with the fact that it is enriched in D and close to a grain boundary, this is possibly a pore. Pores a few nm in size are known from TEM analysis to exist along oxide grain boundaries as discussed previously.

In the “barrier layer”, the observation of D segregation to oxide grain boundaries in this study agree with those previously reported[26,27,49]. Hydroxide formation in the oxide is well-known. Hydroxylated grain boundaries are formed by the breaking of the oxygen bond at the grain boundaries and water molecule splitting, resulting in a H bridge. In the innermost part of the oxide, H atoms or H_2 molecules can enter the metal via an interconnected hydroxylated pathway[50], either through interconnected porosity or oxide grain boundaries, or hydrogen assisted channeling of oxygen vacancies as a route for hydrogen to permeate the barrier oxide resulting in hydrogen pick-up[29]. Our later work on molecular dynamics simulations also reveal that these H_2 molecules can diffuse rapidly through nano-pores and nano-pipes as small as 0.5 nm in the oxide layer[51].

5. Conclusions

In this study, we used a range of complementary high resolution techniques ((S)TEM, Fresnel imaging, TKD mapping, APT and NanoSIMS) to study the oxide formed on Zr-1.0Nb and Zr-2.5Nb from different stages of oxidation: pre-transition, near-transition and post-transition. These samples are either partially deuterated or have undergone full deuterated autoclave corrosion. Our findings are below:

The Zr-1.0Nb has very has even oxide thickness, metal-oxide interface, few cracks and large spacings between layers of transition cracks (2.5~3 μm). TKD mapping shows that it has a more characteristic periodic pattern of equiaxed-columnar grains, with large, elongated columnar grains are oriented parallel to the oxide growth direction, around 50 nm in width and 450~900 nm in length. Post-transition samples have more disorganised oxide grains.

Porosity in the oxide has a major influence on the overall rate of oxidation, and there is much more porosity in the post-transition Zr-1.0Nb alloy than found in pre-transition alloy. This agrees with a previous study suggesting that interconnected porosity is the pathway for corrosion.

1. "barrier layer" porosity has been shown for the first time in high resolution. Depending on the stage of corrosion, the area of 0~200 nm away from the metal-oxide interface is the protective layer. Some of the columnar grain boundaries are seen to be decorated with vertically interconnected porosity where the pores gradually become disconnected as move closer the metal-oxide interface. There are also many individual pores inside the columnar grains, flake-like porosity/micro-cracks around 10-15 nm in width. Individual porosity is also found at the metal-oxide interface and in the suboxide region underneath, which may be a result of agglomeration of the high concentration of oxygen vacancies expected near the metal-oxide interface and can act as an oxygen sink for the local oxidation process. At the end of the columnar grains, there is also continuous porosity that lies at the interface underneath the columnar grains. This kind of complex interconnected porosity seems likely to play an important role in the rate determining oxygen/hydrogen diffusion process.

2. NanoSIMS analysis has shown that at pre-transition there is higher intensities of deuterium in the first 1 μm from the surface, rapidly dropping off further into the oxide. But at post-transition, shows significantly more deuterium throughout the bulk oxide, suggesting that the transition event enables the propagation or trapping of deuterium while the pre-transition sample is a good barrier to deuterium penetration.
3. APT data provides strong direct evidence for D segregation in the "barrier layer" oxide. The features to which D segregates are likely to be oxide grain boundaries even though

co-segregation of Fe at the oxide grain boundary was only observed in one of the analyses. Occasional evidence of porosity with trapped D has also been observed via APT. The pores, if interconnected could be an alternative pathway for hydrogen transport.

4. The results from this work agree with the mechanism involving hydroxylated oxide grain boundaries where H is transported via grain boundaries or nano porosity.

Data availability statement:

The raw/processed data required to reproduce these findings cannot be shared at this time due to legal or ethical reasons.

References

[1] B. Lustman, F. Kerze, The Metallurgy of Zirconium,McGraw-Hill Book Company, Michigan, in: Metall. Zirconium,McGraw-Hill B. Company, Michigan, 1955.

[2] W.E. Berry, Hydrogen Pickup During Aqueous Corrosion of Zirconium Alloys, Corros. Sci. 17 (1961) 109.

[3] B. Cox, A new model for the in-reactor corrosion of zirconium alloys, Int. At. Energy Agency. (1961) 91–110.

[4] D.R. Olander, Fundamental aspects of nuclear reactor fuel elements, 1976. doi:10.2172/7343826.

[5] J. Wei, P. Frankel, E. Polatidis, M. Blat, A. Ambard, R.J. Comstock, L. Hallstadius, D. Hudson, G.D.W. Smith, C.R.M. Grovenor, M. Klaus, R.A. Cottis, S. Lyon, M. Preuss, The effect of Sn on autoclave corrosion performance and corrosion mechanisms in Zr-Sn-Nb alloys, Acta Mater. 61 (2013) 4200–4214. doi:10.1016/j.actamat.2013.03.046.

[6] A. Yilmazbayhan, E. Breval, A.T. Motta, R.J. Comstock, Transmission electron microscopy examination of oxide layers formed on Zr alloys, J. Nucl. Mater. 349 (2006) 265–281. doi:10.1016/j.jnucmat.2005.10.012.

[7] D.R. Olander, A.T. Motta, Waterside Corrosion and Hydriding of Zr Alloy Cladding, 2006.

[8] J. Romero, J. Partezana, R.J. Comstock, L. Hallstadius, Evolution of Hydrogen Pickup Fraction with Oxidation Rate on Zirconium Alloys, TopFuel 2015. (2015) 1–7.

[9] A. Couet, A.T. Motta, R.J. Comstock, Hydrogen pickup measurements in zirconium alloys: Relation to oxidation kinetics, J. Nucl. Mater. 451 (2014) 1–13. doi:10.1016/j.jnucmat.2014.03.001.

[10] J. Wei, P. Frankel, E. Polatidis, M. Blat, A. Ambard, R.J. Comstock, L. Hallstadius, D. Hudson, G.D.W. Smith, C.R.M. Grovenor, M. Klaus, R.A. Cottis, S. Lyon, M. Preuss, The effect of Sn on autoclave corrosion performance and corrosion mechanisms in Zr–Sn–Nb alloys, Acta Mater. 61 (2013) 4200–4214.

[11] S.S. Yardley, K.L. Moore, N. Ni, J.F. Wei, S. Lyon, M. Preuss, S. Lozano-Perez, C.R.M. Grovenor, An investigation of the oxidation behaviour of zirconium alloys using isotopic tracers and high resolution SIMS, J. Nucl. Mater. 443 (2013) 436–443. doi:10.1016/j.jnucmat.2013.07.053.

[12] A. Garner, J. Hu, A. Harte, P. Frankel, C. Grovenor, S. Lozano-Perez, M. Preuss, The effect of Sn concentration on oxide texture and microstructure formation in zirconium alloys, Acta Mater. 99 (2015) 259–272. doi:10.1016/j.actamat.2015.08.005.

[13] J. Wei, P. Frankel, M. Blat, a Ambard, R.J. Comstock, L. Hallstadius, S. Lyon, R. a Cottis, M. Preuss, Autoclave study of zirconium alloys with and without hydride rim, Corros. Eng. Sci. Technol. 47 (2012) 516–528. doi:10.1179/1743278212Y.0000000055.

[14] A. Couet, A.T. Motta, R.J. Comstock, R. Couet, Effect of Alloying Elements on Hydrogen Pickup in Zirconium Alloys, (n.d.) 479–509. doi:10.1520/STP154320120215.

[15] M. Youssef, M. Yang, B. Yildiz, Doping in the Valley of Hydrogen Solubility: A Route to Designing Hydrogen-Resistant Zirconium Alloys, Phys. Rev. Appl. 5 (2016) 014008. doi:10.1103/PhysRevApplied.5.014008.

[16] B.D.C. Bell, S.T. Murphy, R.W. Grimes, M.R. Wenman, The effect of Nb on the corrosion and hydrogen pick-up of Zr alloys, Acta Mater. 132 (2017) 425–431. doi:10.1016/J.ACTAMAT.2017.04.063.

[17] J. Hu, A. Garner, P. Frankel, M. Li, M. Kirk, S. Lozano-Perez, M. Preuss, C. Grovenor, Effect of neutron and ion irradiation on the metal matrix and oxide corrosion layer on Zr-1.0Nb cladding alloys, Acta Mater. (2019). doi:10.1016/j.actamat.2019.04.055.

[18] H.G. Kim, I.H. Kim, B.K. Choi, J.Y. Park, Y.H. Jeong, K.T. Kim, Study of the corrosion and microstructure with annealing conditions of a ??-quenched HANA-4 alloy, Corros. Sci. 52 (2010) 3162–3167. doi:10.1016/j.corsci.2010.05.014.

[19] H.G. Kim, S.Y. Park, M.H. Lee, Y.H. Jeong, S.D. Kim, Corrosion and microstructural characteristics of Zr–Nb alloys with different Nb contents, J. Nucl. Mater. 373 (2008) 429–432. doi:10.1016/j.jnucmat.2007.05.035.

[20] H.G. Kim, Y.H. Jeong, T.H. Kim, Effect of isothermal annealing on the corrosion behavior of Zr-xNb alloys, J. Nucl. Mater. 326 (2004) 125–131. doi:10.1016/j.jnucmat.2004.01.015.

[21] G.J.C. Carpenter, J.A. Jackman, J.P. McCaffrey, R. Alani, In Situ Hydride Formation in Zirconium and Titanium during Ion Milling, Microsc. Microanal. 1 (1995) 175–184. doi:10.1017/S1431927695111757.

[22] B. Cox, Y.M. Wong, Hydrogen uptake micro-mechanism for Zr alloys, J. Nucl. Mater. 270 (1999) 134–146. doi:10.1016/S0022-3115(98)00898-8.

[23] B. Cox, A mechanism for the hydrogen uptake process in zirconium alloys, J. Nucl. Mater. 264 (1999) 283–294. doi:10.1016/S0022-3115(98)00492-9.

[24] B. Cox, F. Gauducheau, W. Yin-Mei, Cathodic sites on Zircaloy surfaces, J. Nucl. Mater. 189 (1992) 362–369. doi:10.1016/0022-3115(92)90389-3.

[25] N. Ramasubramanian, P. Balakrishnan, Aqueous Chemistry of Lithium Hydroxide and Boric Acid and Corrosion of Zircaloy-4 and Zr-2.5Nb Alloys, in: Zircon. Nucl. Ind. Tenth Int. Symp., 2009. doi:10.1520/stp15199s.

[26] M. Lindgren, G. Sundell, I. Panas, L. Hallstadius, M. Thuvander, H.-O. Andrén, Toward a Comprehensive Mechanistic Understanding of Hydrogen Uptake in Zirconium Alloys by Combining Atom Probe Analysis With Electronic Structure Calculations, in: Zircon. Nucl. Ind. 17th Vol., ASTM International, 100 Barr Harbor Drive, PO Box C700, West Conshohocken, PA 19428-2959, 2015: pp. 515–539. doi:10.1520/STP154320120164.

[27] M. Lindgren, I. Panas, Impact of additives on zirconium oxidation by water: mechanistic insights from first principles, RSC Adv. 3 (2013) 21613. doi:10.1039/c3ra42941e.

[28] M. Lindgren, I. Panas, Oxygen Vacancy Formation, Mobility, and Hydrogen Pick-up during Oxidation of Zirconium by Water, Oxid. Met. (2017). doi:10.1007/s11085-016-9695-z.

[29] M. Lindgren, C. Geers, I. Panas, Possible origin and roles of nano-porosity in ZrO2scales for hydrogen pick-up in Zr alloys, J. Nucl. Mater. (2017). doi:10.1016/j.jnucmat.2017.05.017.

[30] N. Ni, S. Lozano-Perez, M.L. Jenkins, C. English, G.D.W. Smith, J.M. Sykes, C.R.M. Grovenor, Porosity in oxides on zirconium fuel cladding alloys, and its importance in controlling oxidation rates, Scr. Mater. 62 (2010) 564–567. doi:10.1016/j.scriptamat.2009.12.043.

[31] N. Ni, Study of Oxidation Mechanisms of Zirconium Alloys by Electron Microscopy, Univ. Oxford. (2011) PhD Thesis.

[32] H. Beie, A. Mitwalsky, F. Garzarolli, H. Ruhmann, H. Sell, Examinations of the Corrosion Mechanism of Zirconium Alloys, in: Zircon. Nucl. Ind. Tenth Int. Symp., ASTM International, 100 Barr Harbor Drive, PO Box C700, West Conshohocken, PA 19428-2959, 1994: pp. 615-615–29. doi:10.1520/STP15212S.

[33] A. Couet, A.T. Motta, A. Ambard, D. Livigni, In-situ electrochemical impedance spectroscopy measurements of zirconium alloy oxide conductivity: Relationship to hydrogen pickup, Corros. Sci. 119 (2017) 1–13. doi:10.1016/j.corsci.2016.12.008.

[34] H. Göhr, J. Schaller, H. Ruhmann, F. Garzarolli, Long-Term In Situ Corrosion

Investigation of Zr Alloys in Simulated PWR Environment by Electrochemical Measurements, in: Zircon. Nucl. Ind. Elev. Int. Symp., ASTM International, 100 Barr Harbor Drive, PO Box C700, West Conshohocken, PA 19428-2959, 1996: pp. 181-181–22. doi:10.1520/STP16173S.

[35] H.M. Nordin, A.J. Elliot, S.G. Bergin, P. Barberis, S.W. Dean, High Temperature Aqueous Corrosion and Deuterium Uptake of Coupons Prepared from the Front and Back Ends of Zr-2.5Nb Pressure Tubes, J. ASTM Int. 7 (2010) 102979. doi:10.1520/JAI102979.

[36] J. Hu, A. Garner, N. Ni, A. Gholinia, R.J. Nicholls, S. Lozano-Perez, P. Frankel, M. Preuss, C.R.M. Grovenor, Identifying suboxide grains at the metal–oxide interface of a corroded Zr–1.0%Nb alloy using (S)TEM, transmission-EBSD and EELS, Micron. 69 (2015) 35–42. doi:10.1016/J.MICRON.2014.10.004.

[37] K. Li, T. Aarholt, J. Liu, H. Hulme, A. Garner, M. Preuss, S. Lozano-Perez, C. Grovenor, 3D-characterization of deuterium distributions in zirconium oxide scale using high-resolution SIMS, Appl. Surf. Sci. (2019). doi:10.1016/j.apsusc.2018.09.101.

[38] J. Hu, A. Garner, N. Ni, A. Gholinia, R.J. Nicholls, S. Lozano-Perez, P. Frankel, M. Preuss, C.R.M. Grovenor, Identifying suboxide grains at the metal-oxide interface of a corroded Zr-1.0%Nb alloy using (S)TEM, transmission-EBSD and EELS, Micron. 69 (2015) 35–42. doi:10.1016/j.micron.2014.10.004.

[39] G. Sundell, THESIS FOR THE DEGREE OF LICENTIATE OF ENGINEERING Atom Probe Tomography of Hydrogen and of Grain Boundaries in Corroded Zircaloy---2, n.d.

[40] R.A. Karnesky, N.C. Bartelt, D. Huang, N. Teslich, M. Kumar, SANDIA REPORT Imaging and Quantification of Hydrogen Isotope Trapping, n.d.

[41] S.B. SETIADINATA, Corrosion and Hydrogen Pickup Mechanisms of Zirconium Alloys, University of Oxford, 2016.

[42] M. Herbig, M. Kuzmina, C. Haase, R.K.W. Marceau, I. Gutierrez-Urrutia, D. Haley, D.A. Molodov, P. Choi, D. Raabe, Grain boundary segregation in Fe-Mn-C twinning-induced plasticity steels studied by correlative electron backscatter diffraction and atom probe tomography, Acta Mater. 83 (2015) 37–47. doi:10.1016/j.actamat.2014.09.041.

[43] G. Sundell, M. Thuvander, A.K. Yatim, H. Nordin, H.O. Andrén, Direct observation of hydrogen and deuterium in oxide grain boundaries in corroded Zirconium alloys, Corros. Sci. (2015). doi:10.1016/j.corsci.2014.10.016.

[44] M. Herbig, M. Kuzmina, C. Haase, R.K.W. Marceau, I. Gutierrez-Urrutia, D. Haley, D.A. Molodov, P. Choi, D. Raabe, Grain boundary segregation in Fe–Mn–C twinning-induced plasticity steels studied by correlative electron backscatter diffraction and atom probe tomography, Acta Mater. 83 (2015) 37–47. doi:10.1016/J.ACTAMAT.2014.09.041.

[45] M. Elmoselhi, B. Warr, S. McIntyre, A Study of the Hydrogen Uptake Mechanism in Zirconium Alloys, in: Zircon. Nucl. Ind. Tenth Int. Symp., ASTM International, 100 Barr Harbor Drive, PO Box C700, West Conshohocken, PA 19428-2959, 1994: pp. 62-62–18. doi:10.1520/STP15184S.

[46] P. Bossis, G. Lelièvre, P. Barberis, X. Iltis, F. Lefebvre, Multi-Scale Characterization of the Metal-Oxide Interface of Zirconium Alloys, in: Zircon. Nucl. Ind. Twelfth Int. Symp., ASTM International, 100 Barr Harbor Drive, PO Box C700, West Conshohocken, PA 19428-2959, 2000: pp. 918-918–27. doi:10.1520/STP14334S.

[47] M. Ramasubramanian, N., Perovic, V. and Leger, Hydrogen transport in the oxide and hydrogen pickup by the metal during out-and in-reactor corrosion of Zr-2.5Nb pressure tube material., in: Zircon. Nucl. Ind. Twelfth Int. Symp. Am. Soc. Test. Mater., 2000.

[48] M.K. Miller, L. Longstreth-Spoor, K.F. Kelton, Detecting density variations and nanovoids, Ultramicroscopy. 111 (2011) 469–472. doi:10.1016/j.ultramic.2011.01.027.

[49] G. Sundell, M. Thuvander, H.-O. Andrén, Hydrogen analysis in APT: Methods to control adsorption and dissociation of H2, Ultramicroscopy. 132 (2013) 285–289. doi:10.1016/J.ULTRAMIC.2013.01.007.

[50] N. Ramasubramanian, Localised electron transport in corroding zirconium alloys, J. Nucl. Mater. 55 (1975) 134–154. doi:10.1016/0022-3115(75)90148-8.

[51] E.M. Jing Hu, Sergio Lozano-Perez, Chris Grovenor, Mikael Christensen, Walter Wolf, Erich Wimmer, Hydrogen pickup during oxidation in aqueous environments: the role of nano-pores and nano-pipes in zirconium oxide films. Under review, Acta Mater. (n.d.).